Structure and Function in Rhodopsin: Mapping Light-Dependent Changes in Distance between Residue 316 in Helix 8 and Residues in the Sequence 60−75, Covering the Cytoplasmic End of Helices TM1 and TM2 and Their Connection Loop CL1[†]

Christian Altenbach,[‡] Judith Klein-Seetharaman,[§,||] Kewen Cai,[§,⊥] H. Gobind Khorana,*[,§] and Wayne L. Hubbell*[,‡]

*Jules Stein Eye Institute and Department of Chemistry and Biochemistry, University of California,
Los Angeles, California 90095-7008, and Departments of Biology and Chemistry, Massachusetts Institute of Technology,
Cambridge, Massachusetts 02139*

ABSTRACT: Double-spin-labeled mutants of rhodopsin were prepared containing a nitroxide side chain at position 316 in the cytoplasmic surface helix H8, and a second nitroxide in the sequence of residues 60−75, which includes the cytoplasmic loop CL1 and cytoplasmic ends of helices TM1 and TM2. Magnetic dipole−dipole interactions between the spins were analyzed to provide interspin distance distributions in both the dark and photoactivated states of rhodopsin. In the dark state in solutions of dodecyl maltoside, the interspin distances are found to be consistent with structural models of the nitroxide side chain and rhodopsin, both derived from crystallography. Photoactivation of rhodopsin shows a pattern of increases in internitroxide distance between the reference, position 316 in H8, and residues in CL1 and TM2 that suggests an outward displacement of TM2 relative to H8 by ≈3 Å.

Site-directed spin labeling (SDSL)[1] is a powerful tool for the investigation of structure and dynamics in proteins of arbitrary molecular weight, both water-soluble and membrane-bound (see refs *1−5* for reviews). In SDSL, substituted cysteine residues are modified with a sulfhydryl-selective reagent to provide a nitroxide side chain. In the studies presented here, the methanethiosulfonate reagent (I) was employed to produce the side chain designated R1 (Figure 1).

In earlier SDSL studies of rhodopsin, the sequence dependencies of R1 solvent accessibility and mobility were
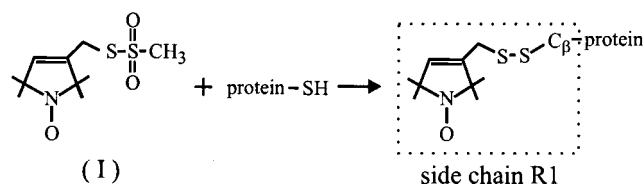

FIGURE 1: Reaction of methanethiosulfonate reagent I with a cysteine to yield side chain R1.

used to deduce the secondary structure and main features of the tertiary fold of the molecule throughout the entire cytoplasmic surface. In addition, patterns of changes in R1 dynamics upon photoactivation revealed a clear rigid-body motion of TM6. Smaller changes were detected in the vicinity of the other transmembrane helices that could also be interpreted in terms of rigid-body movements (*6−14*).

Changes in patterns of R1 mobility can identify a helix movement, but cannot as yet provide a quantitative value for its magnitude. To obtain this information, mapping of interhelical distances and changes upon photoactivation is needed. This is possible in SDSL by using magnetic dipolar interactions between two R1 residues. One such previously reported study investigated the movement in TM6 (*15*). The TM6 displacement due to photoactivation was analyzed after freezing the sample, and found to be ≈8 Å. In a preceding paper (*16*), quantitative analysis of relative movements in the TM1, TM7, H8 helix group at the cytoplasmic surface is reported using magnetic dipolar interactions between R1 pairs at room temperature (*17*).

In the study presented here, distance mapping by magnetic dipolar interactions at room temperature in both the dark and photoactivated states is extended to include the TM1, TM2,

* To whom correspondence should be addressed. W.L.H.: Jules Stein Eye Institute, UCLA School of Medicine, Los Angeles, CA 90095-7008; telephone, (310) 206-8830; fax, (310) 794-2144; e-mail, hubbellw@jsei.ucla.edu. H.G.K.: Departments of Chemistry and Biology, Massachusetts Institute of Technology, Cambridge, MA 02139; telephone, (617) 253-1871; fax, (617) 253-0533; e-mail, khorana@mit.edu.

[‡] University of California.

[§] Massachusetts Institute of Technology.

[||] Current address: Institute for Software Research International, Carnegie Mellon University, Wean Hall 4604, Pittsburgh, PA 15213.

[⊥] Current address: Biogen, Inc., 14 Cambridge Center, Cambridge, MA 02142.

[1] Abbreviations: DM, dodecyl maltoside; EPR, electron paramagnetic resonance; T4L, T4 lysozyme. Mutants with a single spin-label are given the sequence number for the spin-labeled position followed by R1 designations. Thus, 65R1 is the mutant with the R1 side chain at site 65. Double-spin-labeled mutants are designated in a similar fashion; i.e., 65R1+316R1 is the double mutant with R1 side chains at sites 65 and 316.
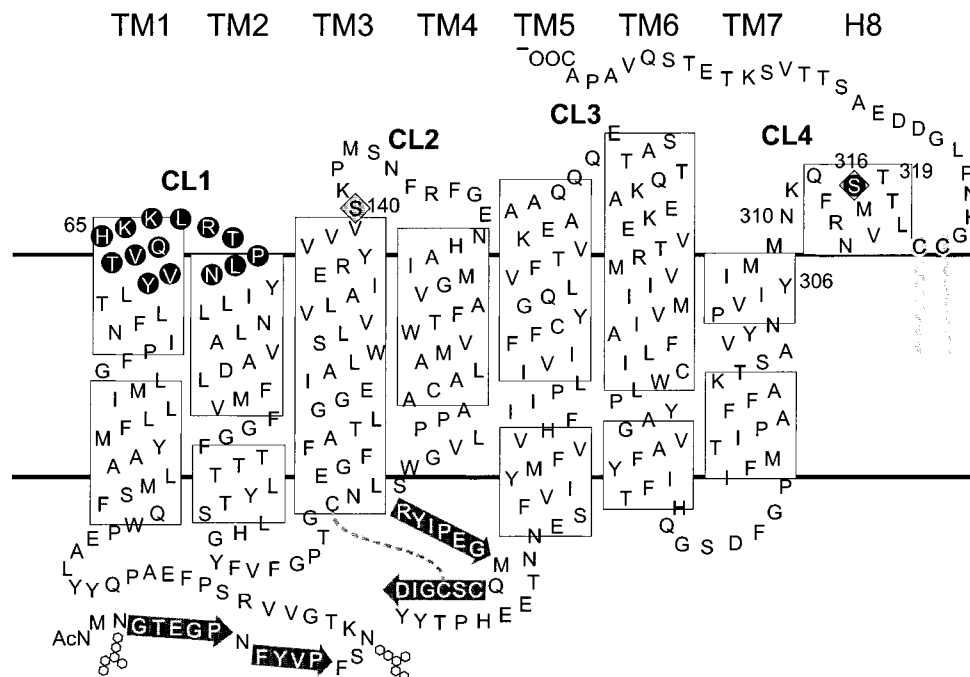
FIGURE 2: Secondary structural model of rhodopsin, highlighting the residues included in this study (black circles). The interhelical loops at the cytoplasmic surface are labeled CL1–CL4. Residue 316 in helix H8 was selected for substitution with one R1 side chain as a reference. A second R1 side chain was placed in the sequence of residues 60–75. Sites at which native cysteine residues were replaced with serine are denoted with diamonds. The secondary structure of CL3 is based on SDSL data (*9*), and that for the remainder of the molecule is derived from a crystal structure (PDB entry 1F88).

H8 helix group, as well as the interconnecting loop CL1 (Figure 2). The general experimental strategy is to introduce one R1 residue at a "reference" site in the protein, together with a second R1 residue that is scanned through a sequence that lies nearby. The resulting set of distances relative to the reference provides a pattern that reflects the local structure. In this approach, it is important to obtain multiple sets of distances to mitigate a potential bias due to the existence of multiple rotamers of the R1 side chain (*17, 18*).

In this study, site 316 in the short surface helix H8 near the cytoplasmic termination of helix TM7 was selected as a reference, and a second R1 placed at positions in the sequence of residues 60–75 that contains the cytoplasmic termination of transmembrane helices TM1 and TM2 and their connecting loop CL1 (Figure 2). The spin–spin interactions that result between the two nitroxides are analyzed from room-temperature data according to methods described in a preceding paper (*17*). The results show that the nitroxide in 316R1 lies within spin–spin interaction range (<20 Å) of a number of residues in the sequence that is being investigated, and for those pairs, internitroxide distance distributions were determined. Modeling of the R1 side chain using configurations established from crystal structures of R1 in T4L (*18*) shows remarkable agreement of the data with a structural model of rhodopsin derived from X-ray crystallographic data refined to 2.8 Å (*19*). This agreement in the dark state structure is important in interpreting the distance changes upon photoactivation in terms of structure changes.

Photoactivation of rhodopsin results in relatively small increases in distance between 316R1 and most R1 residues with which it interacts in the sequence of residues 60–75. Together with data on mobility changes for single R1 residues in the sequence of residues 60–75 (*13*), and the reactivity of substituted cysteines in this sequence (*20*), the

results are interpreted to imply a movement of TM2 away from H8 by a distance ≈3 Å.

EXPERIMENTAL PROCEDURES

Preparation and EPR Spectroscopy of Spin-Labeled Rhodopsin Mutants. The single-cysteine mutants of rhodopsin 60C–75C and 316C were prepared and purified in a DM (Anatrace, Maumee, OH) solution according to published procedures (*6, 20*). The double-cysteine mutants containing 316C and a second cysteine at each of the positions listed above for the single mutants were prepared and purified in DM as described previously (*21*). The mutants were prepared in a base mutant of rhodopsin where the reactive cysteines 140C and 316C were replaced with serine (Figure 2).

The single- and double-cysteine mutants in a DM solution were spin-labeled and the EPR spectra recorded in both the dark and after photoactivation as described in ref *16*. Absorption EPR spectra were obtained by integration of the experimental first-derivative spectra after simple baseline and phase corrections (*17*).

Analysis of EPR Spectra in Terms of Interspin Distances. Analysis of the spectra in terms of the interspin distance between nitroxide pairs in double mutants was carried out as described in a preceding paper (*17*). For completeness, the salient features of the analysis are outlined below. First, the EPR spectrum of the double-labeled mutant is deconvoluted with the average of the EPR spectra of the corresponding single mutants (the hypothetical "noninteracting" spectrum) to give a broadening function characteristic of the interaction (*22*). For dipole–dipole interaction between a pair of spins separated by a fixed distance and randomly oriented with respect to the magnetic field, the function is taken to be the Pake function (*23*). For a distribution of interspin distances, the broadening function is a weighted sum of Pake

functions. The experimentally determined broadening function is fit to a sum of Pake functions with the distance distribution as a parameter. The fit to the broadening function is then convoluted with the noninteracting spectrum to provide a "simulated" spectrum. The agreement between the experimental and simulated spectrum is a measure of the validity of the derived distance distribution. This method holds for nitroxide−nitroxide interactions as long as (1) the nitroxide rings have random orientations with respect to one another, (2) the interspin vector is randomly oriented with respect to the external field, and (3) the interspin vector has a rotational correlation time of ≥20 ns. As discussed previously, the last two conditions hold for rhodopsin in DM micelles (*16*). When both nitroxides are relatively immobilized, the nitroxide rings could assume a fixed orientation with respect to each other, and condition 1 may not hold. In the experiments described here, the reference 316R1 has an immobilized component, and in combination with other sites with immobilized components, effects of relative orientation may occur. However, such effects, if serious, are revealed in the poor agreement of the simulated and experimental spectrum. As shown below, the fits are generally satisfactory for the pairs examined here.

Modeling of the R1 Side Chain in the Rhodopsin Structure. To compare the experimentally measured distances for consistency with the structural model of rhodopsin, the R1 side chains were modeled in the rhodopsin structure essentially as described in a preceding paper (*17*). For the sites studied here, the starting conformation for the R1 side chain was taken to be the g^+g^+ state of the X_1 and X_2 dihedrals, as identified in crystal structures (*18*). The X_3 dihedral (about the S−S bond) was also assigned as a g^+ state to avoid steric interactions with the backbone on helical surfaces. This choice led to unacceptable overlap for residue 61, so an X_1 of 90° was selected here. After all other side chains had been replaced with glycine, the structure was energy minimized with all backbone, $C\beta$, and disulfides atoms of the spin-labels fixed in space, only allowing rotations of the X_4 and X_5 dihedrals. Initially, the experimentally determined distances were used as constraints. Following minimization, the distance constraints were removed, and molecular dynamics simulations were carried out at 450 K for 1000 ps, again with X_4 and X_5 as the only variables. The distance distributions from the dynamics run showed significant overlap with the measured distributions and were thus compatible.

RESULTS

EPR Spectra for the Double-Spin-Labeled Mutants and the Criteria for Spin−Spin Interaction. Figure 3 shows the first-derivative EPR spectra for the double-labeled mutants in the dark (solid trace) and after photoactivation (dashed trace). A static magnetic dipolar interaction between nitroxide spins leads to an increase in overall breadth and a concomitant decrease in the intensity of the EPR spectrum. For near-quantitative labeling of the cysteine residues and strong spin−spin interactions, such dipolar broadening is immediately obvious in the EPR spectrum. For example, in the double mutants 316R1+65R1 and 316R1+73R1, the interaction is clearly revealed in the broad wings of the spectra (arrows).

On the other hand, spin−spin interactions may be difficult to detect by this simple criterion in the presence of a
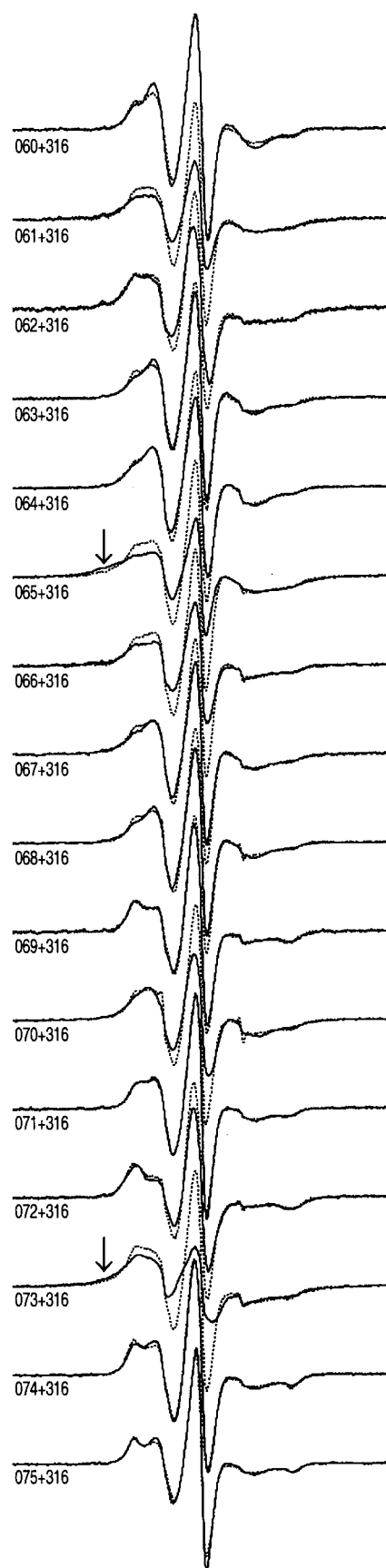

FIGURE 3: Experimental first-derivative EPR spectra of the double mutants in the dark (—) and after photoactivation (···).

significant fraction of noninteracting spins due, for example, to incomplete labeling of the cysteine residues. For the rhodopsin mutants used in this study, incomplete labeling is

often encountered because mild reaction conditions are employed to avoid reaction of the buried, native cysteine residues 167C, 185C, 222C, and 264C (*6*). Hence, the narrow, more intense signal from the noninteracting spins may dominate the broader, less intense features of the magnetically coupled pairs. In such cases, spin–spin interactions may be positively identified in rhodopsin by changes in the intensity of the center resonance line ($m_I = 0$) of the EPR spectrum upon photoactivation, as discussed in a preceding paper (*16*). Using this criterion, which only identifies interactions that change upon photoactivation, spin pairs involving 316R1 and 61R1, 62R1, 65R1, 66R1, 70R1, 72R1, and 73R1 are deemed to lie within spin–spin interaction range (Figure 3).

The absorption EPR spectrum more clearly reveals underlying broad components in the presence of narrow, noninteracting components, particularly when compared with the hypothetical noninteracting state computed as the average of the spectra of the corresponding single mutants (*16*). Panels a and b of Figure 4 show this comparison for each double mutant in the dark and photoactivated states, respectively. As can be seen in Figure 4a, the difference in the absorption spectrum of the double mutant in the dark and its noninteracting counterpart clearly identifies as interacting the same pairs listed above, but in addition suggests a weak interaction in 316R1+67R1. Small differences in other cases are within the errors involved in the integration and normalization procedures used to obtain the absorption spectra. For 316R1+61R1 and 316R1+66R1, the tails on the low-field side of the absorption spectra reveal broad components due to spin–spin interaction (arrows) not visible in the first-derivative spectra. In the other double mutants (316R1 with 60R1, 63R1, 64R1, 68R1, 69R1, 71R1, 74R1, and 75R1), no interactions could be detected by any of the criteria, and these are not further analyzed.

A comparison of the superposed spectra of Figure 4b reveals the strength of the spin–spin interaction in the photoactivated state. It is clear that the spectra of the double mutants now more closely resemble those of the noninteracting state than they did in the dark, indicating that in each case the interaction is weaker and the interspin distance greater. For 316R1+61R1 and 316R1+66R1, the broad components in the tails of the spectra have disappeared.

Analysis of Interacting Spin Pairs in Terms of Distance and Changes with Photoactivation. For each of the interacting pairs at room temperature, distance distributions were computed according to the deconvolution method described in a preceding paper (*17*). Panels a and b of Figure 5 summarize the results of such analyses in the dark and photoactivated states, respectively. As a check on the validity of each distribution, the EPR spectrum simulated from the distribution (dashed trace) is compared with the experimental spectrum of the double mutant. First-derivative spectra are shown here because they provide a more critical assessment of the quality of the simulation than would be afforded by the absorption spectra.

As in previous work, satisfactory simulation of the experimental spectrum required that some fraction of the total spins were effectively noninteracting (f_{NI}), which is at a distance of greater than ~20 Å. This fraction is believed to arise from a population of incompletely labeled protein (*16*). For the sites investigated in the study presented here, 0.06
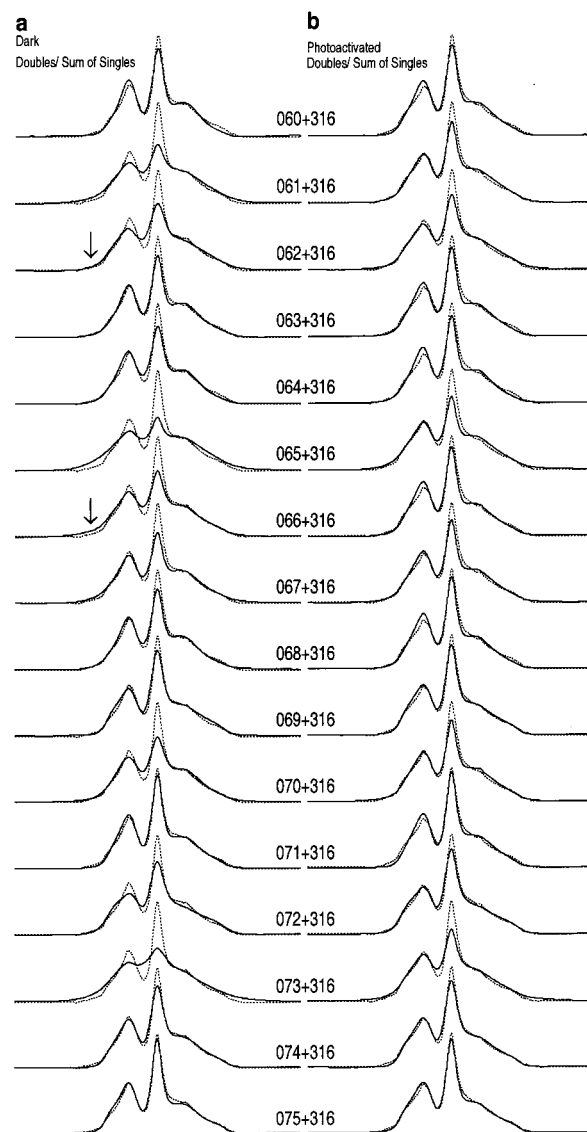

FIGURE 4: Absorption EPR spectra of R1 in rhodopsin. (a) Spectra of the indicated double mutant (dark trace) and the algebraic sum of the spectra of the corresponding single mutants (light trace), both in the dark state. (b) Spectra of the indicated double mutant and the algebraic sum of the spectra of the corresponding single mutants, both after photoactivation at room temperature. The absorption spectra reveal the presence of broad, low-amplitude, underlying components that correspond to close distances in a distribution (denoted with arrows).

$\leq f_{NI} \leq 0.37$. Upon photoactivation, the amount of noninteracting spin increases, primarily reflecting a distance shift such that part of the distribution moves beyond the detection limit.

For the 316R1+61R1 mutant, the distribution shows two interacting spin populations of roughly equal size, with modes near 12 and 16 Å. The noninteracting population is the highest of the pairs studied ($f_{NI} = 0.37$). Upon photoactivation, the modes of the two populations increase by ~3 Å, and f_{NI} increases by 0.24, largely due to the tail of the population at longer distances moving out of range.

In 316R1+62R1, there is a single population with a mode near 16 Å and a distribution extending from ≈15 to 17 Å, with an f_{NI} of 0.28. Upon photoactivation, the mode remains near 16 Å, but the distribution skews to longer distances, extending from 15 to 20 Å. The increase in f_{NI} of 0.14 is

again due largely to the tail of the distribution extending beyond the detection range.

For 316R1+65R1, the results obtained independently in this study agree well with those reported in a preceding paper (*16*). In the dark state, there is a single interacting population with a mode at ~9 Å and an f_{NI} of 0.20. Upon photoactivation, there is a change in the spectral line shape, suggesting a reduction in the level of spin−spin interaction. Analysis reveals that the origin of the change lies in an increase in f_{NI} of 0.20, with the interacting population remaining at about the same distance. The origin of the incremental noninteracting population is unknown, but it is variable, being only 0.06 in the study reported in a preceding paper (*16*). As discussed in ref *16*, it is possible that the incremental noninteracting population arises from the formation of later intermediates in the bleaching process, or is due to local unfolding.

Residues 66−70 lie in the interconnecting loop CL1 between TM1 and TM2 at the cytoplasmic surface of the protein. The 316R1+66R1 and 316R1+67R1 pairs both have similar spectral line shapes and similar bimodal distance distributions in the dark state, with modes at 12 and 17 Å. For the 316R1+70R1 pair, the dark state distance distribution has a mode at 13 Å, and is strongly skewed to longer distances extending beyond the detection limit. For each of these pairs, $f_{NI} \sim 0.20$. Upon light activation, the distance distribution for the 316R1+66R1 pair shifts dramatically, with all distances near or beyond the detection limit. Essentially, the population at longer distances has increased at the expense of the one at shorter distances. The 316R1+67R1 pair is still characterized by modes at 12 and 17 Å, but there is an increase in f_{NI} of 0.12, accounting for the small change in signal amplitude upon bleaching in the first-derivative spectra (Figure 2). The light-induced change in the distance distribution for 316R1+70R1 is similar to that for 316R1+66R1, and the distances shift to near or beyond the detection limit, accounting for a large increase in f_{NI} of 0.41.

Spin pair 316R1+72R1 shows relatively weak interaction in the dark, with an f_{NI} of 0.36, and the remainder in a broad distribution centered near the detection limit at ~18 Å. The spectral intensity changes upon photoactivation (Figure 3) result from a shift in the distribution by ≈3 Å, resulting in an increase in f_{NI} of 0.38.

Finally, the spin pair 316R1+73R1 shows one of the strongest spin−spin interactions in the dark state of the pairs that have been studied. The derived distance distribution reveals two populations with modes at 9 and ~13 Å, and an f_{NI} of 0.06. Upon light activation, the two modes shift by ~3 Å to longer distances, and there is an increase in f_{NI} of 0.13 due to the tail of the longer distance distribution moving out of range.

Comparison of Distance Distributions with the Rhodopsin Structural Model. To check for consistency between the experimental distance distributions and the rhodopsin structural model determined from crystallography (*19*), the R1 side chain was modeled in the rhodopsin structure as described in Experimental Procedures. In the case of bimodal distance distributions, only the mode of the distribution corresponding to the closest distance was used as a constraint to guide the initial energy minimization. In all cases, the

mode of the second distribution could be accommodated by simple rotations about X_4 (not shown).

Remarkably, the results revealed that the experimentally estimated interspin distances were consistent with both the structural model of rhodopsin in the crystal and a single conformation of the R1 side chain where $X_1 = 310°$ and $X_2 = 310°$ (the g^+g^+ conformation), believed to be preferred at helical sites (*18, 24, 25*). For illustration, Figure 6 shows a model of the rhodopsin structure containing each side chain in the g^+g^+ conformation and optimized with respect to X_4 and X_5 variation to simultaneously provide energy minimization and agreement with the experimentally determined distances. The R1 side chains are color-coded according to the estimated internitroxide distance in the model. It is immediately apparent that the side chains for which no interaction was detected with 316R1 are indeed predicted to be the furthest from that reference site (R1 in blue, $r \geq 20$ Å), with one interesting exception, namely, 316R1+68R1 (not shown). Residue L68 projects toward C316 and is sufficiently close that there would be strong steric interaction as well as magnetic dipole interaction in the presence of both R1 residues. As reported above, the spin-labeled product of the double-cysteine mutant 316C+68C shows only weak or little spin−spin interaction. This may be the result of strong steric interaction that permits only one of the two sites to react with the spin-label reagent. Alternatively, reaction of both sites could distort the flexible loop, again due to steric interactions, such that the side chains are far apart.

DISCUSSION

Comparison of the Crystal and Solution Conformations of Rhodopsin in the Sequence of Residues 60R1−74R1. In previous work, the accessibility parameter for collision with dissolved O_2 [$\Pi(O_2)$] was determined for each spin-labeled single mutant in the sequence of residues 60R1−74R1 (*13*). The parameter $\Pi(O_2)$ is proportional to the solvent accessibility of R1, and the sequence dependence of $\Pi(O_2)$ is a signature of the tertiary fold, identifying both regular secondary structure and tertiary contact surfaces (*26*). Thus, comparison of experimental values of $\Pi(O_2)$ with fractional solvent accessibilities computed from the corresponding crystal structure is an excellent means of comparing the protein structure in solution with that in the crystal. Figure 7a shows plots of $\Pi(O_2)$ and fractional solvent accessibility, the latter computed from the rhodopsin crystal structure for the sequence of residues 60−74. The striking similarity of these quantities along the sequence reflects essentially identical folds, each revealing the periodic dependence of the helix−turn−helix motif (Figure 7b).

Structural Changes Due to Photoactivation: Motion of TM2. The data presented above on both inter-residue distances and sequence-dependent $\Pi(O_2)$ values establish the essential similarity of the dark structure in solution and in the crystal in the region that has been investigated. In addition, the rates of reaction of cysteine residues in this sequence with sulfhydryl reagents reflect a similar structure (*20*), as do cross-linking rates of 316C with a second cysteine substituted in the sequence (*21*), although there are some interesting differences due to fluctuations in the protein structure (see below). With these results as a foundation, the
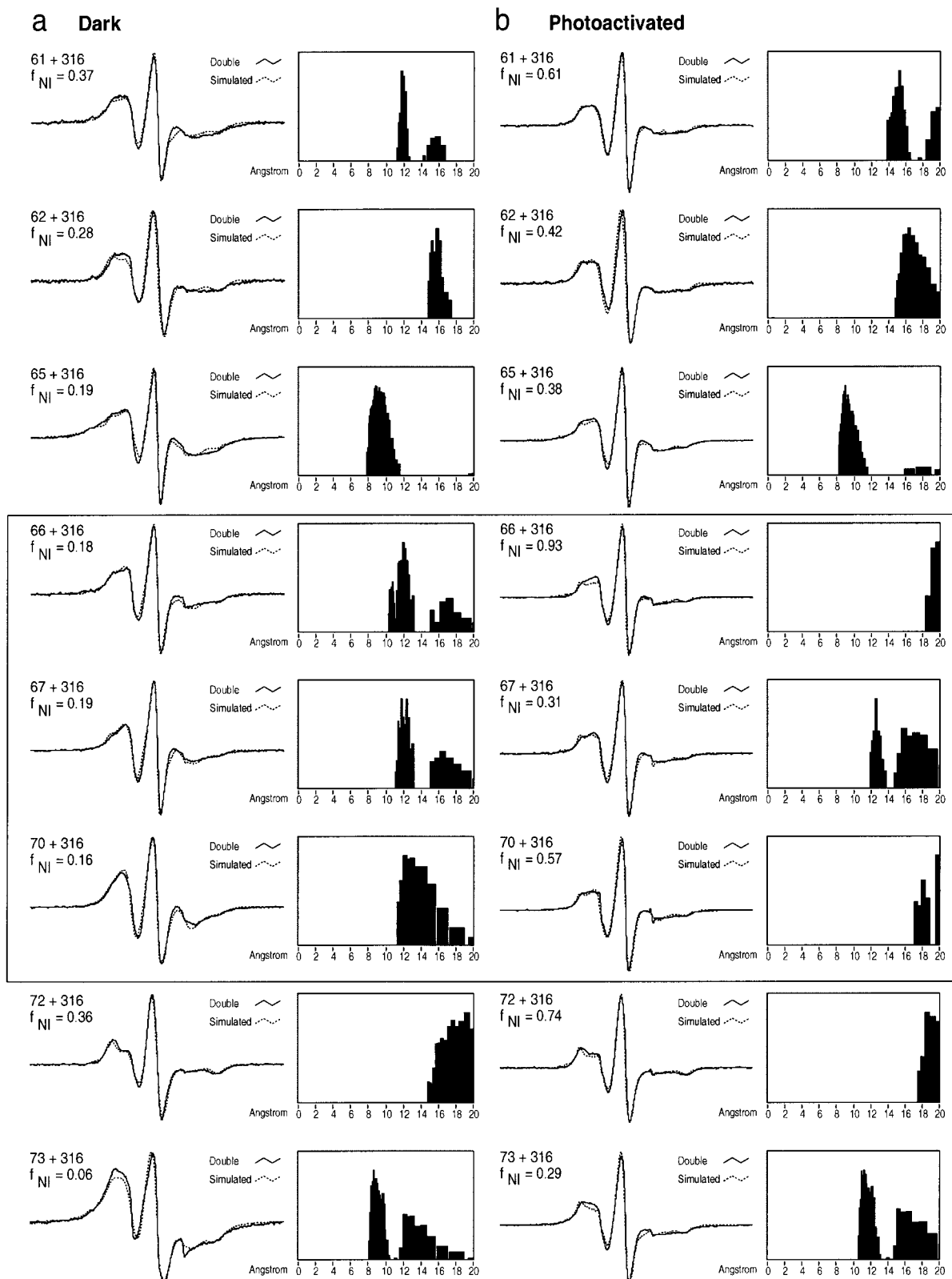
FIGURE 5: Experimental and simulated first-derivative EPR spectra and the derived interspin distance distribution for R1 spin pairs in rhodopsin. (a, left) Experimental first-derivative EPR spectrum of the indicated double mutant in the dark (dark trace) and the simulated spectrum (dotted trace). (a, right) Derived distance distribution in the dark. (b, left) Experimental first-derivative EPR spectrum of the indicated double mutant in the light (dark trace) and the simulated spectrum (dotted trace). (b, right) Distribution of distances after photoactivation. Only interacting spin pairs are included in the figure. The vertical (population) axes of the distributions are arbitrary and selected for convenience of display. The populations of spin pairs with inter-residue distances of >20 Å are not shown, but the fraction of total spin corresponding to these populations (f_{NI}) is given.

major goal of the experiments was to map distance changes in the structure upon photoactivation, and those data are provided in Figure 5.

Earlier studies already revealed changes in structure localized around the cytoplasmic termination of TM2. For example, the rate of reduction of thiopyridinyl derivatives
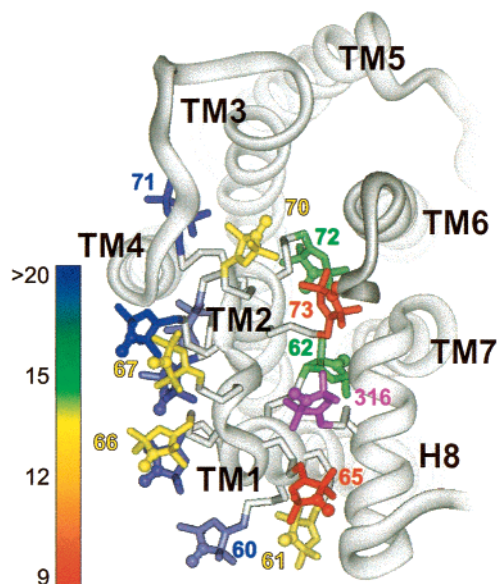
FIGURE 6: Ribbon model of rhodopsin based on a crystal structure (PDB entry 1F88) showing the locations of R1 side chain pairs as stick models. The reference 65R1 is highlighted in violet. The R1 side chains are shown in energy-minimized conformations and are color-coded on the basis of the measured distances.
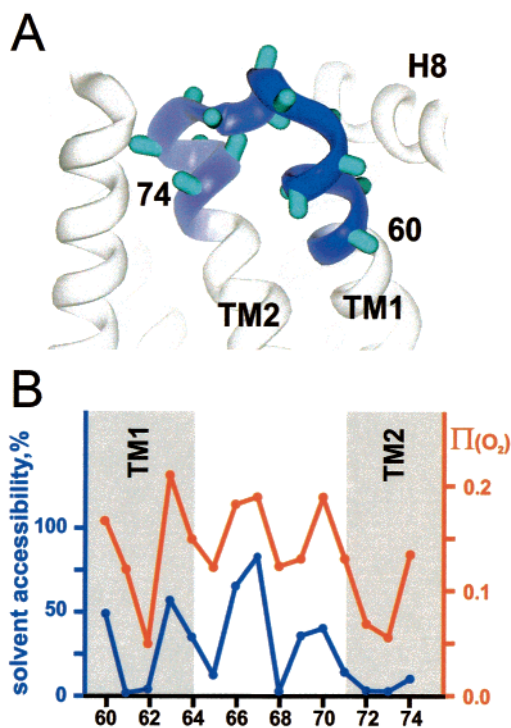

FIGURE 7: (A) Rhodopsin structural model (A chain of PDB entry 1F88, truncated beyond position 323), showing the sequence of residues 60−74. (B) Comparison of the native side chain solvent accessibility, calculated from the crystal structure, and $\Pi(O_2)$ for R1 in the sequence of residues 60−74. Solvent accessibility was calculated using the program MolMol (27).

of cysteine residues 71C−73C with DTT changed dramatically after photoactivation (20). In addition, the mobility of R1 residues 72R1−74R1, distributed around the circumference of TM2, showed a small but reproducible pattern of changes with photoactivation that is consistent with an outward displacement of TM2 toward TM4 (13). The data in Figure 5 show that the distance distribution between the reference 316R1 and sites 72R1 and 73R1 in TM2 shifts to
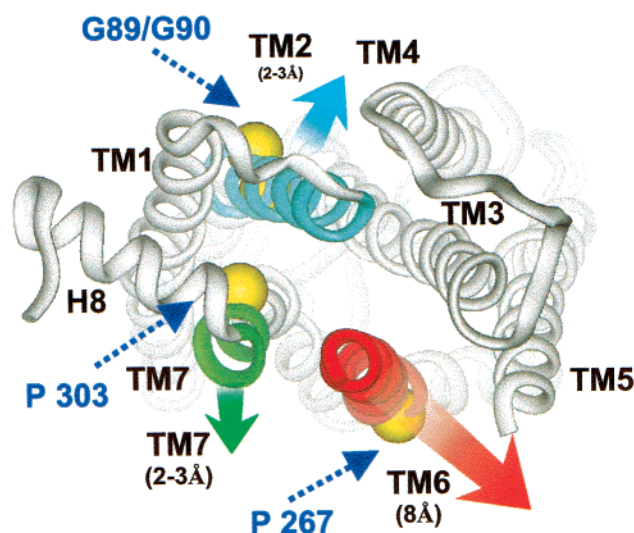

FIGURE 8: Structural model of rhodopsin highlighting the three helical segments found to move during receptor activation. The movements are suggested to be rigid-body tilts approximately in the direction of the arrows and the indicated amplitude. The tilts could result from rotations about "hinge" sites marked by sharp bends at prolines 303 (TM7) and 267 (TM6) and the Gly89/Gly90 pair (TM2).

longer distances by ~2−3 Å upon photoactivation. Taken together, the data suggest a movement of TM2 away from 316R1 by ~2−3 Å, as indicated in Figure 8.

In the model of rhodopsin, TM2 is sharply bent at a Gly89/Gly90 pair (Figure 8), and this pair may provide the hinge for the observed motion. Movement of TM2 can also provide an explanation for the relatively large movements of some R1 residues in CL1 (sites 66 and 70), because changes in backbone dihedral angles in this turn may be necessary to support the motion. In residue 66R1, the large change in distance of up to 8 Å likely results primarily from changes in the side chain position rather than equivalent displacements of the backbone. The data in Figure 5 suggest that the distance change may be interpreted as a conversion of one population into another, perhaps due to small twists in the backbone, or shifts in side chain rotamer equilibria. Similar arguments apply to 70R1.

The interspin distance in 316R1+65R1 changes little upon photoactivation, supporting the conclusion reached in a preceding paper that the cytoplasmic termination of TM1 and the body of helix H8 have a fixed proximity (21).

The relative movements of nitroxides in 316R1+62R1 and 316R1+61R1 are more difficult to interpret in terms of specific protein motions without additional data. Earlier results on the kinetics of reduction of thiopyridinyl derivatives of cysteines in TM1 suggested only small changes in this region upon photoactivation (20). Likewise, the mobility of R1 residues in the sequence of residues 59−65 showed no changes at all upon photoactivation, with the single exception of a small change at 62R1 (13). The changes seen at 62R1 could be coupled to the movement of TM2, because that residue is in direct contact with residues of TM2.

Summary of Structural Changes Detected by SDSL in Rhodopsin Activation. Figure 8 summarizes all of the rigid-body helical movements observed so far by direct distance measurement. Other movements, such as that detected in TM3, were inferred by R1 mobility changes alone, and are

not included in Figure 8. In each case, the movement is in a segment that lies above a hinge site that involves a sharp bend in the helix. The most robust movement is the ≈8 Å displacement of TM6 outward toward residue 227 on TM5 (*9*, *15*). The motion is likely to be generated as a rotation about proline 267 at the bend evident in Figure 8. TM6 appears to be poorly packed with its neighboring helices, a fact which facilitates the large movement without a concomitant rearrangement of the entire tertiary fold of the protein.

In a preceding paper, evidence was presented for the ≈2−4 Å movement, relative to TM1, of a short segment that lies within TM7 just above the retinal binding site at K296. The putative motion could occur with the assistance of a hinge at conserved proline 303, lying just below the segment. Finally, the work presented here is tentatively interpreted as an outward movement of TM2, as shown in Figure 8. This motion may be facilitated by backbone rotations about the Gly89/Gly90 pair at the kink evident in the figure.

Correlation between Disulfide Cross-Linking Rates and SDSL Distance Measurements. In previous studies, disulfide cross-linking rates were investigated in the same double-cysteine mutants used here for attachment of spin-labels for direct distance measurements (*21*). The results showed that the most rapidly cross-linking mutant (316C+65C) was also that in which the spin−spin interaction was the strongest, the results being in good agreement with the crystal structure. Cross-linking rates, spin−spin interactions, and the crystal structure were also in good general agreement for the other double mutants with two notable exceptions. First, 316C+68C had a rapid cross-linking rate, as expected from the proximity in the rhodopsin structure, but no spin−spin interaction was detected. As discussed above, this is attributed to a lack of double labeling due to the strong steric interactions that would exist between two R1 residues at these sites. Second, 316C+73C has a very low cross-linking rate, but the corresponding spin-labeled derivative has a strong spin−spin interaction. In the spin-labeled protein, residue 73R1 projects directly toward 316R1, and the predicted interspin distance is in close agreement with the experimentally measured value. On the other hand, in the double-cysteine mutant, the SH groups are more than twice as distant for disulfide formation. While other cysteine pairs at this distance exhibit measurable cross-linking rates, the tight packing around the buried 73C apparently restricts movement to such an extent that cross-linking is improbable.

REFERENCES

1. Hubbell, W., and Altenbach, C. (1994) *Curr. Opin. Struct. Biol. 4*, 566−573.

2. Hubbell, W. L., Mchaourab, H., Altenbach, C., and Lietzow, M. A. (1996) *Structure 4*, 779−783.

3. Hubbell, W. L., Gross, A., Langen, R., and Lietzow, M. A. (1998) *Curr. Opin. Struct. Biol. 8*, 649−656.

4. Feix, J. B., and Klug, C. S. (1998) in *Biological Magnetic Resonance, Volume 14: Spin Labeling: The Next Millenium* (Berliner, L. J., Ed.) pp 251−281, Plenum Press, New York.

5. Hubbell, W. L., Cafiso, D. S., and Altenbach, C. (2000) *Nat. Struct. Biol. 7*, 735−739.

6. Resek, J. F., Farahbakhsh, Z. T., Hubbell, W. L., and Khorana, H. G. (1993) *Biochemistry 32*, 12025−12031.

7. Farabakhsh, Z., Hideg, K., and Hubbell, W. L. (1993) *Science 262*, 1416−1419.

8. Farahbakhsh, Z. T., Ridge, K. D, Khorana, H. G., and Hubbell, W. L. (1995) *Biochemistry 34*, 8812−8819.

9. Altenbach, C., Yang, K., Farrens, D. L., Farahbakhsh, Z. T., Khorana, H. G., and Hubbell, W. L. (1996) *Biochemistry 35*, 12470−12478.

10. Yang, K., Farrens, D. L., Hubbell, W. L., and Khorana, H. G. (1996) *Biochemistry 35*, 12464−12469.

11. Cai, K., Langen, R., Hubbell, W. L., and Khorana, H. G. (1997) *Proc. Natl. Acad. Sci. U.S.A. 94*, 14267−14272.

12. Altenbach, C., Cai, K., Khorana, H. G., and Hubbell, W. L. (1999) *Biochemistry 38*, 7931−7937.

13. Altenbach, C., Klein-Seetharaman, J., Hwa, J., Khorana, H. G., and Hubbell, W. (1999) *Biochemistry 38*, 7945−7949.

14. Langen, R., Cai, K., Altenbach, C., Khorana, H. G., and Hubbell, W. L. (1999) *Biochemistry 38*, 7918−7924.

15. Farrens, D. L., Altenbach, C., Yang, K., Hubbell, W. L., and Khorana, H. G. (1996) *Science 274*, 768−770.

16. Altenbach, C., Cai, K., Klein-Seetharaman, J., Gobind, H. G., and Hubbell, W. L. (2001) *Biochemistry 40*, 15483−15492.

17. Altenbach, C., Oh, K.-J., Trabanino, R. J., Hideg, K., and Hubbell, W. L. (2001) *Biochemistry 40*, 15471−15482.

18. Langen, R., Oh, K.-J., Cascio, D., and Hubbell, W. L. (2000) *Biochemistry 39*, 8396−8405.

19. Palczewski, K., Kumasaka, T., Hori, T., Behnke, C. A., Motoshima, H., Fox, B. A., Le Trong, I., Teller, D. C., et al. (2000) *Science 289*, 739−745.

20. Klein-Seetharaman, J., Hwa, J., Cai, K., Altenbach, C., Hubbell, W. L., and Khorana, H. G. (1999) *Biochemistry 38*, 7938−7944.

21. Klein-Seetharaman, J., Cai, K., Altenbach, C., Hubbell, W. L., and Khorana, H. G. (2001) *Biochemistry 40*, 12472−12478

22. Rabenstein, M. D., and Shin, Y.-K. (1995) *Proc. Natl. Acad. Sci. U.S.A. 92*, 8239−8243.

23. Pake, G. E. (1948) *J. Chem. Phys. 16*, 327−336.

24. Mchaourab, H. S., Lietzow, M. A., Hideg, K., and Hubbell, W. L. (1996) *Biochemistry 35*, 7692−7704.

25. Columbus, L., Kálai, T., Jekö, J., Hideg, K., and Hubbell, W. L. (2001) *Biochemistry 40*, 3828−3846.

26. Altenbach, C., and Hubbell, W. L. (1997) in *Foundations of Modern EPR* (Eaton, G., Eaton, S., and Salikhov, K., Eds.) pp 423−435, World Scientific Publishing, London.

27. Koradi, R., Billeter, M., and Wüthrich, K. (1996) *J. Mol. Graphics 14*, 51−55.